Electronic Structure of Aqueous $Co[bpy_3]^{2+/3+}$ Electron Mediators

Sreeju Sreekantan Nair Lalithambika,[a,b] Ronny Golnak,[c] Bernd Winter,[d] and Kaan Atak*[,a]

[a] *Institute of Methods for Material Development, Helmholtz-Zentrum Berlin für Materialien und Energie, Albert-Einstein-Strasse 15, 12489 Berlin, Germany*

[b] *Freie Universität Berlin, Fachbereich Physik, Arnimallee 14, D-14195 Berlin, Germany*

[c] *Department of Highly Sensitive X-ray Spectroscopy Helmholtz-Zentrum Berlin für Materialien und Energie, Albert-Einstein-Strasse 15, 12489 Berlin, Germany*

[d] *Department of Molecular Physics, Fritz-Haber-Institut der Max-Planck-Gesellschaft, Faradayweg 4-6, D-14195 Berlin, Germany*

[*] *Corresponding author: kaan.atak@helmholtz-berlin.de*

Abstract

We report on the electronic structure of cobalt (II) tris-2,2'-bipyridine and cobalt (III) tris-2,2'-bipyridine in aqueous solution using resonant inelastic X-ray scattering (RIXS) spectroscopy at the Co L-edge and N K-edge resonances. Partial fluorescence yield X-ray absorption spectra at both edges were obtained by signal integration of the respective RIXS spectra. Experiments are complemented by calculations of the X-ray absorption spectra for high and low spin configurations using density functional theory/restricted open shell configuration interaction singles and time-dependent density functional theory methods. We find that linear combinations of the simulated X-ray absorption spectra for different spin states reproduce the experimental spectra. Best agreement is obtained for measurements at the Co L-edge, for both samples. For cobalt (II) tris-2,2'-bipyridine our combined experimental and computational study reveals ~40% low-spin and ~60% high-spin state components. Much stronger low-spin character is found for cobalt (III) tris-2,2'-bipyridine, ~80% low spin and ~20% high spin. Prominent energy-loss features in the Co RIXS spectra are indicative of d–d excitations and charge-transfer excitations due to strong mixing between metal and ligand orbitals in both complexes. Analysis of N 1s RIXS data reveals the emission from metal dominated orbitals in the valence region, supporting the strong metal–ligand mixing.

Introduction

In the quest for earth-abundant materials for sustainable renewable energy applications, compounds with cobalt-active centers have been extensively investigated over the past decades.[1] Applications ranging from magnetic materials,[2] catalysts, and electrode materials, to specific photo-active centers functional in water splitting and dye-sensitized solar cell systems use cobalt containing complexes as main ingredients.[3–5] Among those complexes, tris(2,2'-bipyridine) cobalt is of particular interest because it assumes two oxidation states, $[Co(bpy)_3]^{2+}$ and $[Co(bpy)_3]^{3+}$, serving as electron mediators in water splitting and in dye-sensitized solar cell systems.[6–8] This redox ability is directly linked to the metal–ligand bonding.[9] In a broader context, the electronic structure of these materials characterized by hybridization, charge transfer and spin-state, plays a crucial role in determining the chemical function in such a multi-component system. Despite the large application potential of these materials, information on the electronic structure is rather scarce, especially in aqueous phase which reasonably well mimics the ambient conditions that exist in a working solar cell or a water-splitting catalytic reactor.[6,7]

Co metal centers (Co^{2+} and Co^{3+}) reported here are octahedrally surrounded by chelating 2,2'-bipyridine ligands which can act as pi-acceptor and sigma-donor, thus forming a stable bond with the metal center.[9] Due to the large ligand size, steric constraints[10] will lead to some deviation from perfect octahedral symmetry, and this can affect the overall stability of the complex. Upon an external stimulus the complexes can switch spin, commonly referred to as spin cross-over.[11] This spin effect is due to the details of the valence electronic structure. The metal centers in the $[Co(bpy)_3]^{2+}$ and $[Co(bpy)_3]^{3+}$ complexes have d^7 and d^6 ground-state configurations with spin adjustability $\Delta S = \pm 1$ and $\Delta S = \pm 2$, respectively. It has been found that structural changes are stronger in the case of $\Delta S = \pm 1$ spin change resulting from the strong Jahn-Teller distortions, particularly for d^7 low-spin configuration.[12]

In the present study we analyze the various possible spin states of the $[Co(bpy)_3]^{2+}$ and $[Co(bpy)_3]^{3+}$ complexes in aqueous solution by a combination of resonant inelastic X-ray scattering (RIXS) spectroscopy [13] and electronic-structure calculations. We report Co L-edge (2p3d) and N K-edge (1s2p) RIXS spectra, and we also present the respective signal-integrated spectra as a function of excitation photon energy which yields the so-called partial fluorescence yield X-ray absorption (PFY-XAS) spectra. The experimental approach is similar to our recent RIXS studies from Co (III) protoporphyrin IX chloride[14] and hemin[15] in solution, where we provided a comprehensive interpretation of PFY-XAS and RIXS spectra with the assistance of electronic structure calculations. Furthermore, and analogous to the previous works, we have simulated the Co $L_{2,3}$-edge XAS, RIXS, and N K-edge RIXS spectra using the density functional theory/restricted open shell configuration interaction singles (DFT/ROCIS) method. We also simulated the

N K-edge XAS spectra using time-dependent density functional theory (TDDFT) method provided by ORCA[16] software package. This allows for an assignment of the spin character.

1. Methods

1.1. Experiments

In order to achieve a sufficiently high concentration of the hydrophobic Co tris-bipyridine complexes[17] we dissolved $[Co(II)(bpy)_3]Cl_2$ and $[Co(III)(bpy)_3]Cl_3$ salts in water to obtain 100 mM and 200 mM concentrations, respectively. Salts were purchased from *Dyenamo Chemicals* (purity > 95%). Aqueous solutions were prepared immediately prior to the RIXS measurements by dissolving the salts in Milli Q water.[18] The RIXS measurements at the Co L-edge and N K-edge for both samples were conducted using the LiXEdrom 2.0 experimental station at the U49-2 PGM1 beamline of the BESSY II synchrotron light facility in Berlin. Liquid samples were contained in a flow-cell equipped with a 150 nm thick SiC membrane separating liquid from vacuum. The flow-cell was connected to a syringe pump (sample volume inside the syringe was ca. 30 ml) operated in push-pull mode with a flow rate of 3 ml/min. Fresh liquid sample was introduced for the Co and N edge measurements. The transmissivity of the membrane was approximately 10% for 400 eV photons, and 65% for 800 eV photons at 45° incidence angle with respect to the beamline. A continuous circulation of the liquid inside the flow-cell is maintained by the syringe pump which minimizes sample damage upon X-ray irradiation. The LiXEdrom 2.0 setup consists of an X-ray spectrometer with two high-resolution variable-line-spacing (VLS) gratings optimized for 200-500 eV (1200 lines/mm) and 500-1200 eV (2400 lines/mm) energy range, respectively. The detector consists of a combination of a microchannel plate (MCP)/ phosphorous screen/ CCD camera assembly. The scattering geometry is set to 90° angle with respect to the incident light direction. Detailed description of the experimental setup can be found elsewhere.[19]

1.2. Computation

We used ORCA software package for the calculations.[16] M06[20] density functional method along with def2-TZVP(-f) basis set[21] was used for molecular geometry optimizations. Transition energies and moments for the Co L-edge were calculated with DFT/ROCIS using the same basis set and B3LYP[22,23] functional. For the N K-edge, TDDFT method was employed, again using the same functional and basis set. For DFT/ROCIS calculations, we applied the B3LYP functional with the parameters c_1=0.18, c_2=0.20, and c_3=0.40.[24] During the calculations, the resolution of identity[25–29]

approximation was used employing the def2-TZV/J auxiliary basis set.[30] Numerical integrations during the DFT calculations were performed on a dense grid (ORCA grid 4). L-edge and K-edge absorption spectra were obtained by applying a 0.8 eV Gaussian-type broadening on each transition moment respectively. The geometry calculations had no symmetry constraint. In all calculations, the relativistic effects were taken into account using zeroth order regular approximation (ZORA).[31] The solvent effects were accounted for using the conductor-like polarizable continuum model (CPCM water) in ORCA.[32]

2. Results and discussion

2.1. Experimental

Geometry optimized molecular structures for both complexes are demonstrated for the low-spin case in Figure 1. The small deviations from octahedral symmetry are quantified by the bond angles and bond lengths shown in Table SI-1 of the Supporting Information (SI). Figure 1 also presents the electronic levels of $3d^6$ and $3d^7$ valence configurations for high spin (HS) and low (LS) spin states. Judged from the Co–N distances and the respective bond angles (Table SI-1), we observe that LS (S=0) case of the $[Co(bpy)_3]^{3+}$ has the highest degree of local octahedral symmetry. Largest deviations from octahedral symmetry are observed for the LS (S=1/2) case of $[Co(bpy)_3]^{2+}$ and for the intermediate spin-state (IS, S=1) case of the $[Co(bpy)_3]^{3+}$, not included in Figure 1. LS case of $[Co(bpy)_3]^{2+}$ has the valence occupation $t_{2g}^6e_g^1$, *i.e.*, with an uneven occupation in the e_g level, causing strong Jahn-teller distortion. In the IS case of the $[Co(bpy)_3]^{3+}$ the ground-state configuration is $t_{2g}^5e_g^1$ with uneven occupations in both t_{2g} and e_g levels which also causes a significant distortion.

Figure 2 presents the experimental Co L-edge (Figures 2a, 2c) and N K-edge (Figures 2b, 2d) PFY-XAS spectra of 100 mM $[Co(bpy)_3]^{2+}$ and 200 mM $[Co(bpy)_3]^{3+}$ aqueous solutions. All spectra are obtained by integrating the individual RIXS spectra signal intensities as a function of excitation photon energy; the actual RIXS spectra will be discussed separately. We first consider the Co 2p PFY-XAS spectra. In the $[Co(bpy)_3]^{2+}$ case (Figure 2a) the spectrum exhibits five noticeable features: a small pre-peak at 776.4 eV (label A_1), a split main peak at 778.4 eV (A_2) and 779.4 eV (A_3), a shoulder near 781.2 eV (A_4), and a broad featureless peak at 793.6 eV (A_5). In contrast, the Co XA spectrum from $[Co(bpy)_3]^{3+}$ (aq) (Figure 2c) exhibits a strong single main absorption peak at 780.6 eV (labeled $\underline{A}_3$) which is at almost the same energy as A_3 for $[Co(bpy)_3]^{2+}$ (aq). Two small absorption pre-peaks occur at 776.6 eV ($\underline{A}_1$) and 779.2 eV ($\underline{A}_2$), a small post-edge peak is seen at 783.4 eV ($\underline{A}_4$), and a stronger band is found at 794.8 eV ($\underline{A}_5$). A_5 and $\underline{A}_5$ correspond to the L_2 edge of the XAS spectra; note the slightly higher energy and smaller peak width of A_5.

The striking differences between the Co 2p PFY-XA spectra from $[Co(bpy)_3]^{2+}$ (aq) and $[Co(bpy)_3]^{3+}$ (aq) can be primarily assigned to the differing 3d-3d coulomb repulsions whereas spin mixing due to spin orbit coupling and the various degrees of valence 3d splitting are arguably playing roles. In the $[Co(bpy)_3]^{2+}$ case, the possible spin states are S = 0.5, for LS, and 1.5 for HS. For the $[Co(bpy)_3]^{3+}$, S can assume values 0 (LS), 1 (IS) and 2 (HS), and yet the IS is less probable. Previous studies[33,34] report the occurrence of IS when an external stimulus, such as temperature variation is applied.[35] For IS to occur, the e_g level has to split strongly enough to overcome exchange interactions which requires considerably large deviation from the octahedral symmetry, but this is rarely encountered for the ground state.[36] A detailed quantitative interpretation of the spectra based on electronic-structure calculations will be provided in section 2.2.

We next discuss the measured N 1s PFY-XAS spectra from $[Co(bpy)_3]^{2+}$ (aq) and $[Co(bpy)_3]^{3+}$ (aq) which again provide insight into the metal–ligand interaction, but now directly probing the ligand. Results are shown in Figures 2b, 2d. Unlike the Co 2p XAS spectra, the N 1s XA spectra are very similar for the two oxidation states and hence there is negligibly small sensitivity to above-observed Co spin behavior; we will make a very similar observation in our electronic structure calculations. In both cases, a strong narrow absorption band appears near ~400 eV excitation energy, accompanied by two smaller post-peaks and a broad absorption band with maximum near 406 eV. For $[Co(bpy)_3]^{2+}$ (aq) (Figure 2c) the specific positions are: 396.5 eV (B_1), 397.4 eV (B_2), 400.0 eV (B_3), 401.8 eV (B_4), and 406.2 (B_5). Absorption bands for $[Co(bpy)_3]^{3+}$ (aq) (Figure 2d) are: 396.4 eV ($\underline{B}_1$), 398.0 eV ($\underline{B}_2$), 399.4 eV ($\underline{B}_3$), 402.2 eV ($\underline{B}_4$), and 406.2 eV ($\underline{B}_5$). B_2 and $\underline{B}_2$ bands are the N 1s→π* transitions characteristic for the bipyridine ring, specifically of the C=N π* unoccupied orbitals.[37] The broad B_5 and $\underline{B}_5$ bands are attributed to the σ* resonance.[38] Bands B_3, B_4, $\underline{B}_3$, $\underline{B}_4$ correspond to the 1s→π* higher-order orbital transitions, possibly exhibiting some metal character. In contrast, the small B_1, $\underline{B}_1$ bands are argued to exhibit considerable metal character as we show in 3.2. Notably, a similar feature has been reported for lanthanide quinoline molecule,[39] in a case where cobalt is not the central metal, where this feature was argued to be due to Co–N bonding states. A full spectral analysis based on computations will be presented in 2.2.

Although the XAS spectra presented in Figure 2 can be considered characteristic fingerprints of each molecule, it is equally instructive to analyze the underlying RIXS spectra from which the XAS spectra are obtained. We first look at the Co 2p data from the two solutions. The full RIXS maps – presenting signal intensities on the excitation photon energy versus emitted photon energy grid – are shown in Figure 3a for $[Co(bpy)_3]^{2+}$ (aq), and in Figure 3c for $[Co(bpy)_3]^{3+}$ (aq). Few selected RIXS spectra, which are horizontal cuts through Figures 3a, 3c, from both solutions are presented in Figures 3b, 3d, respectively. In order to obtain reasonably good signal statistics, the individual RIXS spectra were separately measured for longer

acquisition times (approximately 30 min) as compared to the fast sweeps (approximately 1 min) that lead to the maps presented in Figures 3a and 3c. Note that intensities of the RIXS spectra (Figures 3b, 3d) are normalized to maximum intensity for better visualization of spectral features.

The RIXS maps (Figures 3a, 3c) are found to be fairly similar for the two species but few important differences should be pointed out. In both cases a constant-energy emission in the 765 - 785 eV region is observed for excitation energies from 775-782 eV. This is the 3d→2p fluorescence channel. The band maxima correspond to the absorption bands A_1 to A_4 and $\underline{A}_1$ to $\underline{A}_4$ (of Figure 2a and 2b), respectively. Several weaker photon signals, although barely noticeable in the RIXS-map presentation, identify the resonating energy-loss features, known as Raman emission channels or local excitations.[40 41] These include the d–d excitations and charge transfer excitations of the Raman scattering. Main differences between the two RIXS maps is the larger signal from the Raman channels, responsible for the low-energy tail, most clearly seen at the $\underline{A}_3$ excitation in Figure 3c. For a more quantitative analysis of the actual RIXS features, which also includes assignment of the elastic peak (the recombination due to elastic transitions to the ground state), we need to consider the actual RIXS spectra (Figures 3b, 3d) in order quantify these contributions. These spectra are presented on the energy-loss scale where zero energy corresponds to the elastic peak (black dashed line). Such representation permits an effortless way of displaying final state effects (Raman features). The Raman features occur at constant energy losses with respect to the elastic peak. Hence, aforementioned d–d excitations and charge transfer (CT) excitations occur at the same loss energy, respectively. The former emissions appear within the blue-shaded energy region (at approximately ~1-4 eV energy loss), and the latter contribute within the red-shaded region (between ~7-11 eV in Co^{2+} and ~5.5-12 eV in Co^{3+} systems) marked in Figure 3b, 3d. The larger width of the CT band in Co^{3+} (Figure 3d) results from a larger number of probable transitions compared to the Co^{2+} case. This is due to the higher charge state of the Co^{3+} complex causing a stronger Coulomb attraction between the metal center and the ligands than for the Co^{2+} case. Hence, larger orbital overlap will lead to stronger metal–ligand bonds which manifests by more intense CT transitions. This interpretation would be in agreement with theoretical UV-Vis studies on $[Co(bpy)_3]^{2+/3+}$ in acetonitrile and in the gas phase,[42] where the larger width has been attributed to ligand-to-metal electron transfer**.** Arrows in Figures 3b, 3d mark the positions of the fluorescence (3d→2p channel) which are the features that move with the excitation energy (compare Figures 3a, 3c).

The RIXS spectrum from the Co^{2+} complex measured at the A_1 (776.4 eV; red spectrum) resonance, Figure 3b, shows the main emission at ~1 eV. This band exhibits a weak shoulder at ~2 eV which is the d–d excitation (within blue shade). In addition, a small band is seen at ~8.4 eV loss energy (red shade) which is due to CT excitations. Upon increasing the excitation energy to A_2 (778.4 eV; green spectrum) the spectrum

exhibits a broad structured asymmetric tail between ~0.9 and 3.4 eV, again identifying the d–d transitions. As for A_1 excitation, a small CT band occurs although at the slightly larger loss energy of ~9 eV. Excitation at A_3 (779.4 eV; blue spectrum) results in a similarly asymmetric peak. However, the elastic peak (dashed line) is now more separated from the d–d emission occurring between ~1 and 4 eV. The small CT peak is seen to appear at ~9.4 eV. Excitation A_4 (781.8 eV; magenta spectrum), *i.e.*, above the main resonances, exhibits the same principle energy-loss behavior although the overall spectral shape appears to be quite different, characterized by an increased fluorescence emission near 4 eV relative to the d–d emission at ~2.5 eV, and by a tail structure which is due to CT excitations, at ~9 eV.

For the Co^{3+} system (Figure 3d), resonant excitation at $\underline{A_1}$ (776.4 eV; red spectrum) results in a spectrum with maximum intensity centered at ~1 eV, resembling the one at A_1 excitation of Co^{2+}, except for the CT band (red shade) now extending to higher loss energies. Also, the d–d feature at ~2 eV (blue shade) is less prominent compared to the Co^{2+} system. The spectrum measured at $\underline{A_2}$ (778.8 eV) excitation exhibits pronounced d–d loss signal between ~1.5 and 4.5 eV. CT bands are responsible for the long low-intensity tail (within the red shade). At excitation $\underline{A_3}$ (780.4 eV; blue spectrum) the d–d signal intensity, centered at ~3 eV, is seen to increase relatively to the other bands. Also, the CT signal contribution, now observed between ~6 and 9 eV, is found to increase in intensity. Finally, the RIXS spectrum measured at excitation $\underline{A_4}$ (783.4 eV; magenta trace) exhibits a d–d double peak, at 2.8 and 4.5 eV. A strong CT feature is observed in the 5 – 12 eV loss region. Summarizing Figure 3, we make the following conclusions and comments: (i) the experimental assignment of spectral regions to d–d and CT transitions is rather tentative (based on previous results from similar systems[14]), and there is no clear-cut boundary between these contributions. This requires theoretical calculations as we will discuss below. (ii) Also based on previous works,[14,15] we expect that both cobalt complexes studied here adopt two different spin states which correspond to different valence electron occupations (compare Figure 1). This will be indeed corroborated by our computations. (iii) The lower-energy tails of the individual RIXS spectra gain in intensity as the excitation energy increases which can be associated with the opening of favorable electron delocalization channels (especially intramolecular electron transfer to the ligands) when populating higher-lying d states. (iv) Larger signal intensities of the CT tails observed for Co^{3+} species as compared to their Co^{2+} counterparts would be in accordance with the higher charge on Co^{3+}, and aforementioned accompanying stronger metal-ligand orbital mixing.

Before examining the respective N 1s RIXS spectra a short comparison of the above Co 2p RIXS spectra with our previous studies on Co (III) protoporphyrin IX chloride (Co L-edge) and hemin (Fe L-edge) in solution is beneficial.[14,15] In both earlier studies, the RIXS spectra are dominated by constant-energy

emission (fluorescence) features, and contributions from Raman-type emission are minor. Possibly, this difference is due to the closed-shell valence-structure character. It would thus appear that in the case of open-shell systems (where the unpaired electrons are localized on the metal center) in the present study, at least for $[Co(bpy)_3]^{2+}$ where both possible spin states are expected to be open-shell, the energy-dispersive channel becomes quite favorable. Arguably, for the $[Co(bpy)_3]^{3+}$ case, this may imply that the spin state is not purely LS (zero spin) but rather mixed with a HS component. This is indeed in accordance with our spin-state analysis to be presented below. It is not clear though what exactly causes the increased probability of the Raman channel, an effect that seems to not have been explicitly addressed in the literature. Note that for the same open-shell system N 1s (ligand) core-excitation exhibit only minor Raman-type features. Another noteworthy observation is the relatively strong CT spectral contribution for the cobalt bipyridines as compared to cobalt protoporphyrin IX. This is indicative of strong metal – ligand orbital mixing and will be also detailed later.

We next address the N K-edge RIXS planes and selected RIXS spectra shown in Figure 4. The former data are presented in Figures 4a and 4c for the two Co complexes, respectively, and the individual spectra are shown in Figures 4b and 4d. Unlike in the case of the Co L-edge RIXS spectra, the RIXS spectra in Figures 4b, 4d are displayed on the same energy scale as the RIXS maps, *i.e.*, as a function of the actual emission energy. The RIXS maps from $[Co(bpy)_3]^{2+}$ and $[Co(bpy)_3]^{3+}$ are seen to be very similar in agreement with our expectation that the ligand is rather insensitive to the metal spin state. Both maps exhibit two main emissions (fluorescence) at the constant energies 390.0 and 393.0 eV for excitation photon energies larger than 400 eV. In addition, there is a single sharp absorption at 397.0 eV excitation energy, and the emission is slightly red-shifted as indicated by the red-dashed lines in Figure 4a and 4c; this is seen between excitation energies B_2 (397.4 eV) and B_4 (401.8 eV). Unlike the Co 2p spectra the N 1s RIXS spectra exhibit minor Raman-type features; this is the reason why Figures 4b and 4d are not presented as energy losses. Analogous to our analysis of the Co L-edge RIXS data (Figure 3) we now consider several selected RIXS spectra, at the resonance energies B_2 (397.4 eV), B_4 (401.8 eV), B_5 (406.4 eV) in Figure 4b, and $\underline{B}_2$ (398.0 eV), $\underline{B}_4$ (402.4 eV), $\underline{B}_5$ (406.2 eV) in Figure 4d as this is more suitable to detail spectral differences. Each spectrum has been acquired over longer time, as explained before, and intensities are displayed to yield same heights at maximum. Note that the resonance energies considered in Figure 4 are the same ones already mentioned in Figure 2. In addition, two non-resonant X-ray emission spectra obtained at 420.0 eV for Co^{2+} (Figure 4b) and 410.0 eV for Co^{3+} are presented. Arrows in Figures 4b, 4d now (unlike in Figures 3b, 3d) mark the position of the elastic peaks (corresponding to direct filling of the N 1s core hole).[43] As already expected from the RIXS map of $[Co(bpy)_3]^{2+}$ the RIXS spectra are almost the same for the energies B_4 to B_5, exhibiting the two emissions at 390.0 and 393.0 eV, and the spectral energy shift of the emission band (at

389.0 and 391.4 eV) for B_2 excitation is now clearly visible. We observe a peak at 393.3 eV for B_2 excitation, which moves to 394.5 eV for subsequent excitations from B_4, B_5 and at 420.0 eV (blue dotted line in Figure 4b), a similar pattern can be observed in Co^{3+} case, but is less distinct and only appears as a weak shoulder (blue dotted line in Figure 4d). RIXS spectra of $[Co(bpy)_3]^{3+}$ in Figure 4d exhibit broader spectral features compared to $[Co(bpy)_3]^{2+}$. Most notable is the double-peak structure occurring at emission energies 390.0 eV and 391.7 eV (marked by the pink dotted lines) for the resonant excitation at $\underline{B_2}$ (398.0 eV). Excitation at $\underline{B_4}$ (402.4 eV) shifts the peak to 390.2 eV and 393.0 eV, exhibiting the similar resonance behavior as B_4 excitation in $[Co(bpy)_3]^{2+}$. Excitation at $\underline{B_5}$ (406.2 eV) results in a spectrum which is very similar to the off-resonant X-ray emission spectra measured at 410.0 eV. To both the high and the low-energy side all RIXS spectra exhibit long tails. We also note that the small signal at slightly lower energies of the elastic peaks (red arrows in RIXS maps) are due to vibronic excitations,[44,45] which are however not resolved here. The two intense emission channels (pink lines) can be attributed to emissions from ligand 2p→N 1s transitions. Low-energy tail signal, below 388.0 eV, can be assigned to ligand p →N 1s transitions and s →N 1s transitions;[46] these assignments are supported by our non-resonant X-ray emission spectra calculations (see Figure S2). Those calculations also help in identifying the high-energy peaks marked by blue dotted lines. Our computations suggest that the high-energy section of the emission originates from hybridized Co 3d (t_{2g})-ligand 2p orbitals, with ~53% metal character for Co^{2+} and ~30% for Co^{3+} to be detailed below.

2.2. Computations

We used DFT/ROCIS and TDDFT level of theory to generate the Co L-edge and N K-edge XAS spectra using first principles calculations for a detailed interpretation experimental PFY-XAS spectra. Our aim is to trace the origin of peaks observed in Figure 2. This section starts with a summary of the various computational aspects that we will consider. Our approach enables to calculate XAS spectra with varying constraints such as calculation for different spin states, inclusion of spin orbit coupling and solvent effect. These are the parameters that can be readily accessed within ORCA. Both Co L-edge and N K-edge XAS spectra for different oxidation states were calculated with different spin configurations (LS and HS, also an intermediate spin (IS) for oxidation state +3), shown in Figures 5 and 6. In Figure 7, the doubly/singly occupied candidate (ground state) orbitals obtained from single point DFT calculations for resonant/non-resonant emissions are presented. These orbitals exhibit Co 3d character with varying degrees, some having considerable metal–ligand mixed character. Note that the orbitals displayed in Figures 7, selected due to their significant cobalt character based on Löwdin[47] population analysis, correspond to the highest absorption/emission probabilities.

We also applied the DFT/ROCIS[48] method in an attempt to calculate the RIXS planes of LS configurations of $[Co(bpy)_3]^{2+}$ and $[Co(bpy)_3]^{3+}$. Although the results, presented in Figure S3 and Figure S4, do reasonably well reproduce a pre-peak in Co^{2+} and an extended Raman feature in Co^{3+} across the resonance we note that due to the high computational demand not all the MOs which would play a role in the core-hole deexcitation could be included. Hence, the complete range of RIXS spectra including both d–d and CT transitions cannot be obtained. Nevertheless, in a future study, we intend to calculate the RIXS planes of such complexes with a more comprehensive set of MOs using the new and more efficient PNO-ROCIS/DFT method.[49]

Figure 5 presents the comparison of different computed Co L-edge XAS spectra of $[Co(bpy)_3]^{2+}$ (Figure 5a) and $[Co(bpy)_3]^{3+}$ (Figure 5b). In each figure the top tier shows the experimental spectra (red). Then, in Figure 5a, from top to bottom, we present computed (DFT/ROCIS) XA spectra, for mixed spin-state (black), S = 1.5 (green), and S = 0.5 (blue). For the Co^{3+} case, Figure 5b, we show computed XA spectra for S = 2 (green), S = 1 (purple), and S = 0 (blue). Note that all the calculated XA spectra are normalized according to their highest intensity peaks, and shifted equally to higher energies (12.17 eV for $[Co(bpy)_3]^{2+}$ and 10.7 eV for $[Co(bpy)_3]^{3+}$) in order to match the energies of the experimental spectrum; this is a common procedure to bypass DFT issues with absolute transition energies.[24] It is immediately seen that none of the pure-spin-state calculations matches the experimental spectra. However, rather good agreement is obtained for mixed spin states. For $[Co(bpy)_3]^{2+}$ case a close match to the experimental spectrum (except for the L_3 edge) is obtained when summing up 43% of low spin (S = 0.5) and 57% of high spin (S = 1.5) computed spectra (the relative intensities of the computed spectra are preserved during the summation). The situation is similar for $[Co(bpy)_3]^{3+}$ where the experimental spectrum is reasonably well reproduced by summing up 80% of low-spin (S = 0) and 20% of high-spin (S = 2) computed spectra. It is noted that in the case of $[Co(bpy)_3]^{3+}$ the highly improbable intermediate spin state (S=1) has not been considered in the analysis. We conclude that the electronic ground state is in a single quantum chemical state consisting of mixed spin configurations.[50]

Analogous results are shown for the experimental and computed N 1s XAS spectra for the two cobalt complexes in Figure 6. Reasonable matches with experimental spectra for both $[Co(bpy)_3]^{2+}$ (Figure 6a) and $[Co(bpy)_3]^{3+}$ (Figure 6b) are found for the computed spectra when the same spin components from the Co-analysis are being summed according to the above scheme. As pointed out in the experimental PFY-XAS section of the nitrogen K-edge, the experimental spectra for both species are nearly the same. We make the same observation for the computed spectra: neither the oxidation nor the spin states create significant differences. This insensitivity of the ligand nitrogen atoms toward the oxidation and the spin-state can be

rationalized by the fact that molecular charge and spin are largely governed by the Co-3d originating orbitals which are significantly localized on the central metal atom.

We next assign the XAS features in Figures 5 and 6 with the help of our calculations but we restrict to the most important transitions relevant for LS and HS configurations. Assignment is based on analyzing the DFT/ROCIS output for XA transitions.[51] Note that DFT/ROCIS is capable to account for 2p – 3d and 3d – 3d multiplet structure and incorporation of spin orbit coupling by configuration interactions.[51]

$[Co(bpy)_3]^{2+}$ Co 2p XAS spectra: According to our computational model absorption bands A_1 and A_2 originate from the HS state, and A_3 from the LS state. The pre-edge feature A_1 is associated with the 2p→3d (t_{2g}) transition. This part of the spectrum is hence sensitive to the singly occupied molecular orbital (SOMO) of the molecule in HS configuration. The most intense peak A_2 is associated with 2p→3d (e_g) transitions; the 3d (e_g) orbitals are singly occupied in the HS ground state. Absorption A_3 arises mainly from the LS state of the Co^{2+} (blue spectrum in Figure 5a). In LS configuration, this transition is associated with 2p→3d (e_g) transitions. The small band A_4, also reproduced in the same computed LS spectrum, can be assigned to metal-to-ligand charge transfer (MLCT) transitions.

$[Co(bpy)_3]^{3+}$ Co 2p XAS spectra: The strong A_3 band originates mainly from the LS configuration, corresponding to 2p→3d (e_g) transitions. The small low-energy features $\underline{A}_1$ and $\underline{A}_2$ are absent in the calculated LS spectrum, and are suggested to only occur for the HS state of the complex. Indeed, the calculated spectrum for the HS configuration (green spectrum in Figure 5b) reproduces absorptions $\underline{A}_1$ and $\underline{A}_2$. They can be attributed to 2p→3d t_{2g}, e_g transitions. The HS calculation also reproduces the main feature $\underline{A}_3$ with a weak intensity. $\underline{A}_4$ is the MLCT transition, already mentioned for the Co^{2+} complex.

$[Co(bpy)_3]^{2+}$ and $[Co(bpy)_3]^{3+}$ N 1s XAS spectra: Nitrogen 1s absorptions B_1 to B_4 and $\underline{B}_1$ to $\underline{B}_4$ are dominated by the π-electron system of 2,2'-bipyridine, leading to 1s→π* transitions. The broad features B_5 and $\underline{B}_5$ are assigned to transitions into σ* shape resonance, a quasi-bound level caused by a hump in the potential shape.[38]

Our calculations for LS (S = 0.5) show that the characteristic π* resonance at B_2 is due to the promotion of the N 1s electron to the ligand dominated orbitals of the molecule. In molecules with a pyridine ring structure, the intense π* peak arises from C=N bonds.[37] Our Löwdin[47] analysis for both spin states suggests that the absorbing orbital is formed from the hybridized Co (e_g) and N 2p orbitals with a Co 3d type orbital contribution of approximately 3%.

The small absorption feature $\underline{B_1}$ (396.4 eV) arises from the HS component only; the LS XAS calculation (blue) does not reproduce the pre-edge feature. This feature corresponds to a transition from N 1s to the SOMOs, with main contribution from Co 3d e_g (≈65%) orbitals. Both LS and HS XAS calculations reproduce the intense peak $\underline{B_2}$. Both our LS and HS XAS calculations identify the $\underline{B_2}$ feature as occurring from the N 1s to ligand dominated orbitals with ≈95% contribution by N and C atoms.

Conclusions

Our combined experimental and computational (soft-X-ray) RIXS study at the Co 2p and the nitrogen 1s edges from the cobalt electron-mediator complexes, $[Co(bpy)_3]^{2+}$ and $[Co(bpy)_3]^{3+}$, enables a good quantification of the mixed metal–ligand valence orbitals that are crucial for electron delocalization and thus intramolecular charge transfer. Our DFT/ROCIS calculations of Co 2p X-ray absorption spectra for different spin states are capable to well reproduce experimental spectra; the latter are obtained from the signal integration of the RIXS spectra. In particular, we can reasonably quantify the relative metal-to-ligand character of the most relevant orbitals in the RIXS process by linear combinations of calculated XA spectra for different pure-spin states. The observed stronger low-spin character (80% *versus* 20% high spin) for the $[Co(bpy)_3]^{3+}$ complex, compared to $[Co(bpy)_3]^{2+}$ (43% low-spin, 57% high-spin), can be understood in terms of the relative stability of a low spin $3d^6$ configuration. An important aspect of the present study is that our analysis of the electronic structure explicitly involves the detailed interpretation of the actual RIXS spectra. This provides additional information on the specific molecular states involved, fully based on experiment. With that we determine for instance that the larger signal intensities of the CT tails (in the RIXS spectra) observed for Co^{3+} species as compared to their Co^{2+} counterparts are in accordance with the higher charge on Co^{3+}, which is connected with stronger metal–ligand orbital mixing. We also quantitatively interpreted the measured N K-edge XAS spectra assisted by theoretical calculations. As expected for the large bipyridine ligands, the differences in metal charge and spin state are not reflected in the respective ligand-based excitations. Both experimental and computed spectra (for the various spin states) are almost the same for the two Co complexes. In summary, we have demonstrated the large potential of RIXS, specifically of RIXS-inferred XAS spectra and actual RIXS spectra, for the investigation of transition metal (metal center) complexes with large sensitivity to spin states. We also discussed challenges in the computations, exemplified here by the limitations of DFT/ROCIS calculations to reproduce all prominent details of the RIXS maps.

Supporting Information available: Table showing bond angles and bond lengths, N XES calculations and comparison with experiments, Co L-edge and N K-edge RIXS calculations.

Acknowledgments

K. A. acknowledges financial support of the Einstein Foundation Berlin for a postdoctoral scholarship. S.S.N.L. acknowledges the EMINTE PhD. Scholarship from the European commission. We thank the HZB for the allocation of synchrotron radiation beamtime.

Figures

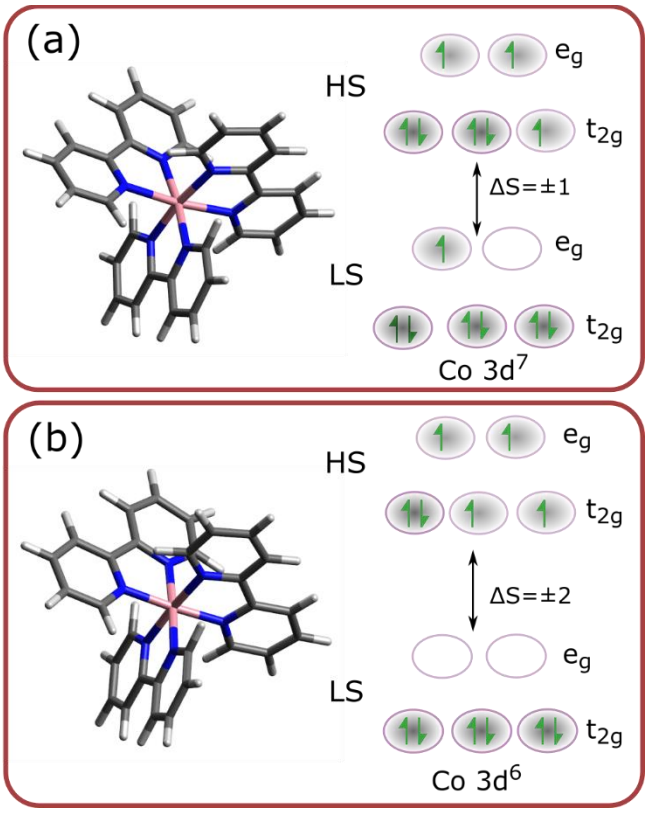

Figure 1

DFT (def2-TZVP(-f)/M06/CPCM water) optimized geometries of (a) $[Co(bpy)_3]^{2+}$ and (b) $[Co(bpy)_3]^{3+}$. Pink, blue, and light grey colors represent Co, N and H atoms, respectively. Possible spin configurations in the valence 3d orbitals, both high spin (HS) and low spin (LS) are also shown.

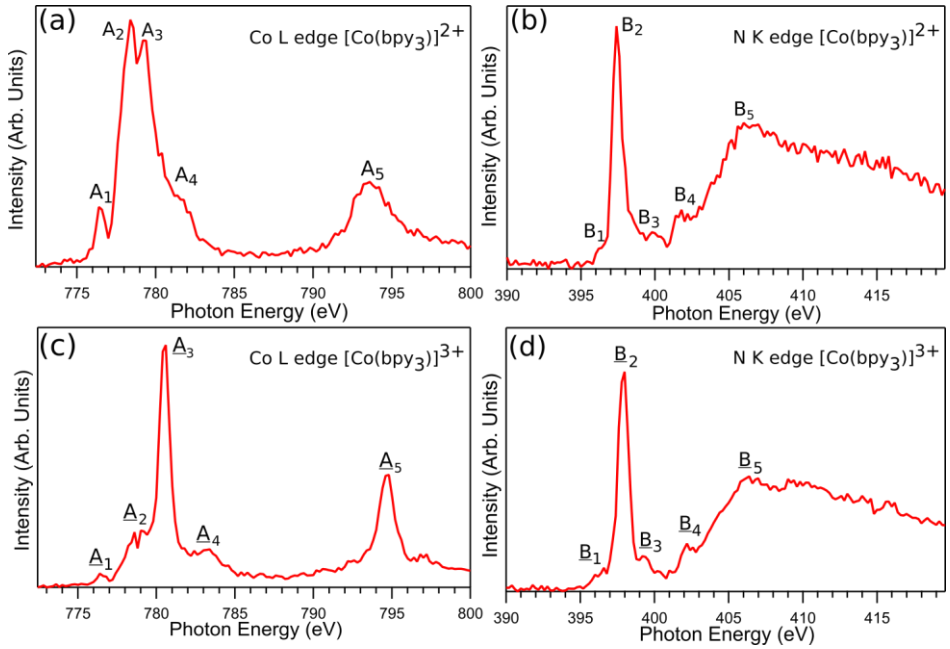

Figure 2

Experimental (a) Co L-edge spectra from 100 mM $[Co(bpy)_3]^{2+}$ and (c) and 200 mM $[Co(bpy)_3]^{3+}$ aqueous solutions; N K-edge PFY-XAS spectra from the same solutions: (b) 100 mM $[Co(bpy)_3]^{2+}$ and (d) and 200 mM $[Co(bpy)_3]^{3+}$. Prominent spectral features are labeled A_1 to A_5, $\underline{A}_1$ to $\underline{A}_5$, B_1 to B_5 and $\underline{B}_1$ to $\underline{B}_5$.

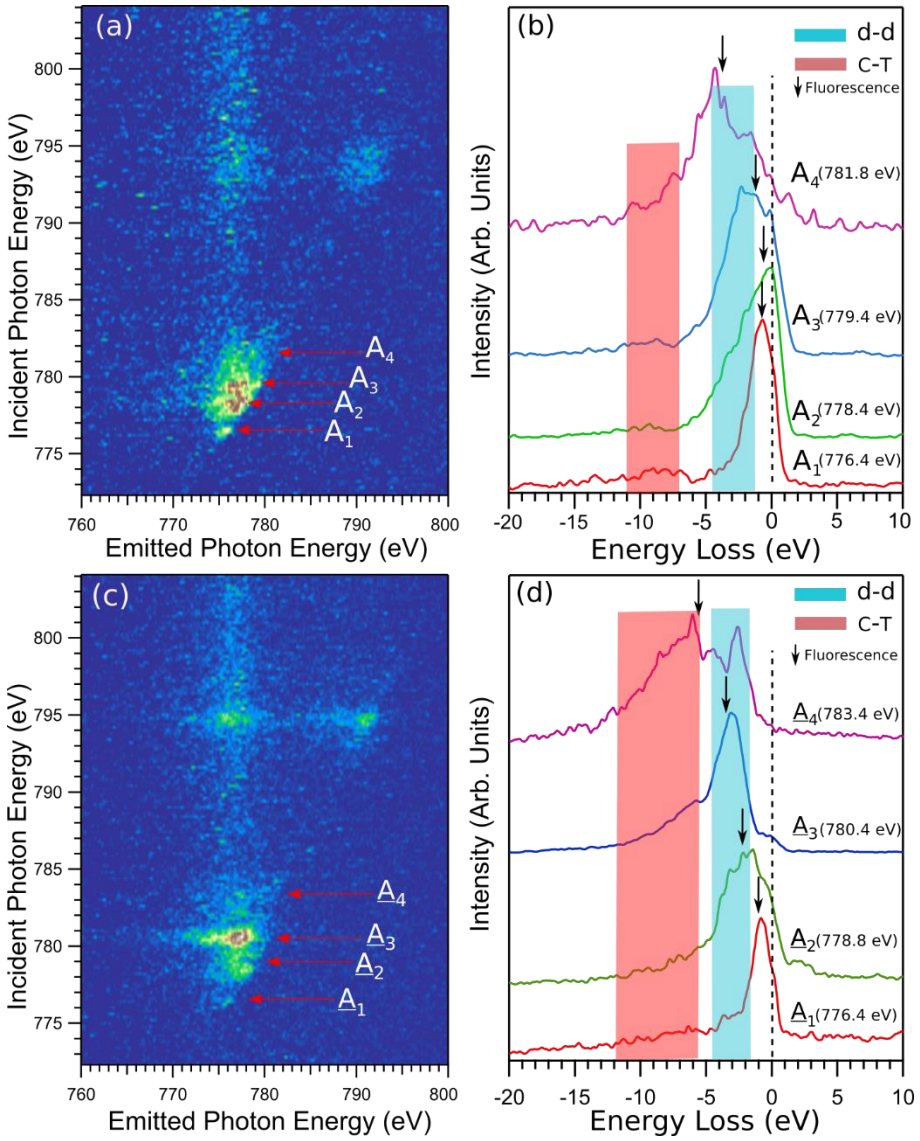

Figure 3

(a) Co L-edge RIXS map and (b) selected RIXS spectra from 100 mM $[Co(bpy)_3]^{2+}$ aqueous solution. (c) RIXS map and (d) RIXS spectra from 200 mM aqueous $[Co(bpy)_3]^{3+}$ solution. Individual RIXS spectra in (b) and (d) have been collected for longer times; see main text. RIXS spectra, (b) and (d), are presented on the energy-loss axis; in this presentation the fluorescence features (marked by arrows) are not a constant energy. Intensities are shown such that the respective maxima have the same peak heights for each tier.

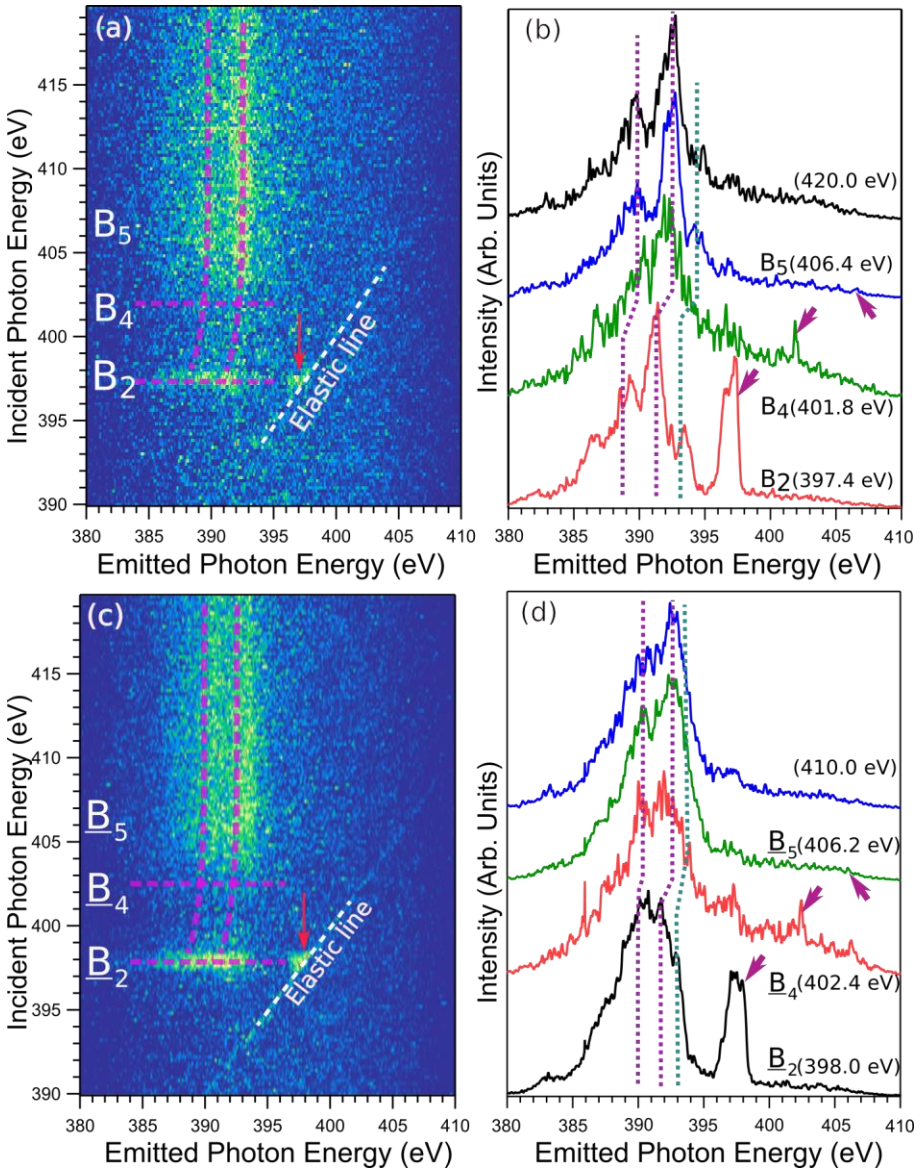

Figure 4

(a) and (b) present the N K-edge RIXS map and RIXS spectra from 100 mM $[Co(bpy)_3]^{2+}$ aqueous solution. (c) and (d) show the RIXS map and RIXS spectra from 200 mM aqueous $[Co(bpy)_3]^{3+}$ solution. As in Figure 3, RIXS spectra were collected for longer times, and intensities are displayed to yield same heights at maximum. The slanted dotted lines in the RIXS maps highlight the position of the elastic peaks; they are marked with arrows in the individual RIXS spectra.

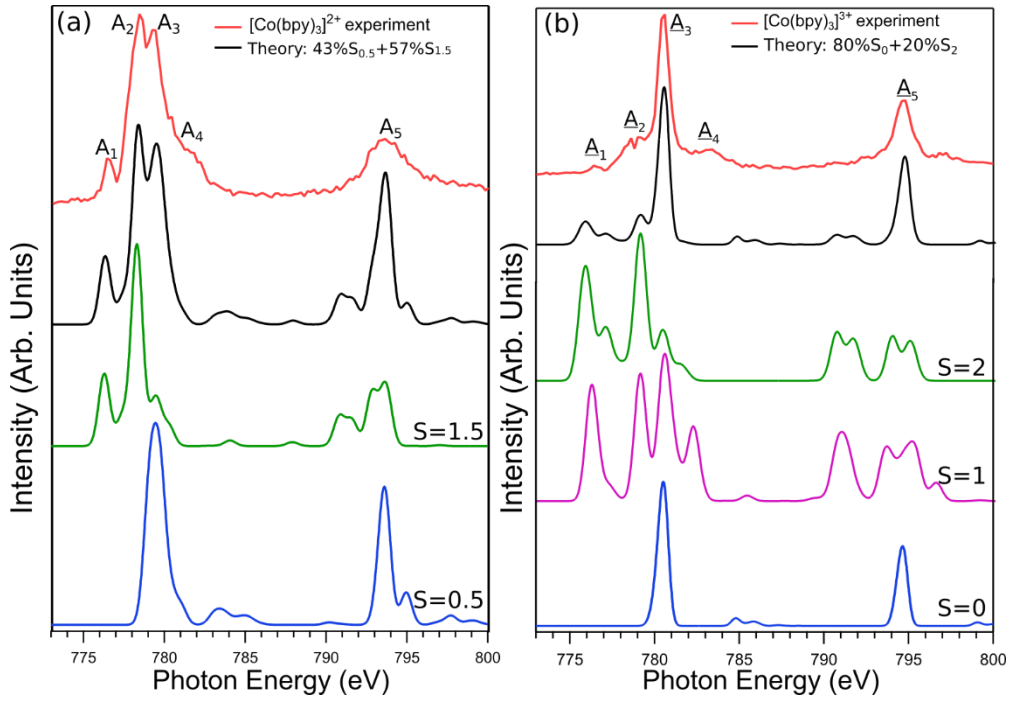

Figure 5

Computed Co L-edge XAS spectra of (a) $[Co(bpy)_3]^{2+}$ and (b) $[Co(bpy)_3]^{3+}$ complexes using DFT/ROCIS with different possible spin and mixed-spin configurations; the various spin states used in the calculations are explained by the color codes. Aqueous environment is implemented by enabling the conductor-like polarizable continuum model (CPCM). Experimental spectra are shown for comparison on the top, in red.

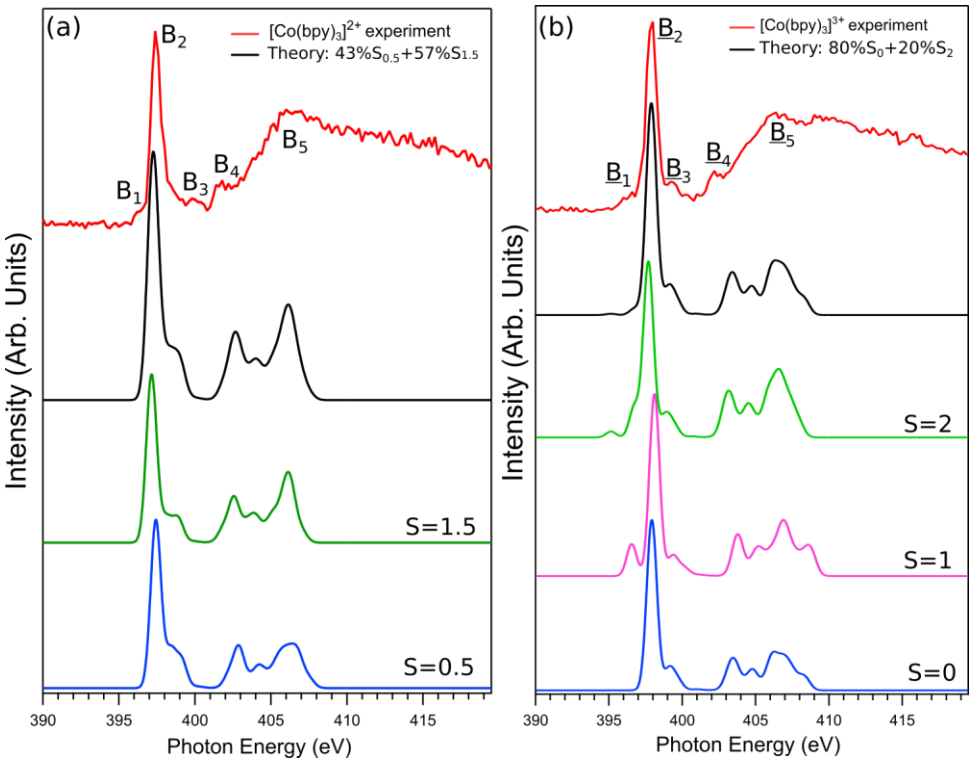

Figure 6

Computed N K-edge XAS spectra from (a) $[Co(bpy)_3]^{2+}$ and (b) $[Co(bpy)_3]^{2+}$ complexes using TDDFT with different spin configurations. Labels and color codes are analogous to Figure 5. Also, the mixed-state spectrum (in black) has been obtained with the same spectral ratios as in Figure 5.

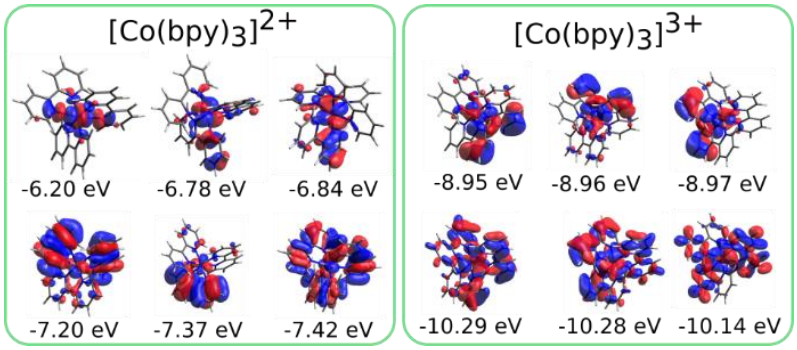

Figure 7

Candidate orbitals for RIXS with significant Co 3d and ligand 2p contributions obtained from ground state single point DFT calculations employing B3LYP functional with def2-TZVP(-f) basis set for $[Co(bpy)_3]^{2+}$ and $[Co(bpy)_3]^{3+}$ in LS configuration.

References

(1) Artero, V.; Chavarot-Kerlidou, M.; Fontecave, M. Splitting Water with Cobalt. *Angew. Chem. Int. Ed.* **2011**, *50* (32), 7238–7266. https://doi.org/10.1002/anie.201007987.

(2) Zhang, X.-M.; Li, C.-R.; Zhang, X.-H.; Zhang, W.-X.; Chen, X.-M. Unusual Slow Magnetic Relaxation in Helical Co3(OH)2 Ferrimagnetic Chain Based Cobalt Hydroxysulfates. *Chem. Mater.* **2008**, *20* (6), 2298–2305. https://doi.org/10.1021/cm7032542.

(3) Yella, A.; Lee, H.-W.; Tsao, H. N.; Yi, C.; Chandiran, A. K.; Nazeeruddin, M. K.; Diau, E. W.-G.; Yeh, C.-Y.; Zakeeruddin, S. M.; Grätzel, M. Porphyrin-Sensitized Solar Cells with Cobalt (II/III)–Based Redox Electrolyte Exceed 12 Percent Efficiency. *Science* **2011**, *334* (6056), 629–634. https://doi.org/10.1126/science.1209688.

(4) Krishnan, C. V.; Sutin, N. Homogeneous Catalysis of the Photoreduction of Water by Visible Light. 2. Mediation by a Tris(2,2'-Bipyridine)Ruthenium(II)-Cobalt(II) Bipyridine System. *J. Am. Chem. Soc.* **1981**, *103* (8), 2141–2142. https://doi.org/10.1021/ja00398a066.

(5) Krishnan, C. V.; Brunschwig, B. S.; Creutz, C.; Sutin, N. Homogeneous Catalysis of the Photoreduction of Water. 6. Mediation by Polypyridine Complexes of Ruthenium(II) and Cobalt(II) in Alkaline Media. *J. Am. Chem. Soc.* **1985**, *107* (7), 2005–2015. https://doi.org/10.1021/ja00293a035.

(6) Feldt, S. M.; Gibson, E. A.; Gabrielsson, E.; Sun, L.; Boschloo, G.; Hagfeldt, A. Design of Organic Dyes and Cobalt Polypyridine Redox Mediators for High-Efficiency Dye-Sensitized Solar Cells. *J. Am. Chem. Soc.* **2010**, *132* (46), 16714–16724. https://doi.org/10.1021/ja1088869.

(7) Sasaki, Y.; Kato, H.; Kudo, A. $[Co(Bpy)_3]^{3+/2+}$ and $[Co(Phen)_3]^{3+/2+}$ Electron Mediators for Overall Water Splitting under Sunlight Irradiation Using Z-Scheme Photocatalyst System. *J. Am. Chem. Soc.* **2013**, *135* (14), 5441–5449. https://doi.org/10.1021/ja400238r.

(8) Sun, Z.-Z.; Zheng, K.-M.; Li, Q.-S.; Li, Z.-S. Rational Design of Co-Based Redox Mediators for Dye-Sensitized Solar Cells by Density Functional Theory. *RSC Adv.* **2014**, *4* (60), 31544–31551. https://doi.org/10.1039/C4RA04605F.

(9) Atkins, P. *Shriver and Atkins' Inorganic Chemistry*; OUP Oxford, 2010.

(10) Miessler, G. L.; Fischer, P. J.; Tarr, D. A. *Inorganic Chemistry*; Pearson Education, Limited, 2014.

(11) Gütlich, P.; Gaspar, A. B.; Garcia, Y. Spin State Switching in Iron Coordination Compounds. *Beilstein J. Org. Chem.* **2013**, *9*, 342–391. https://doi.org/10.3762/bjoc.9.39.

(12) Halcrow, M. A. The Effect of Ligand Design on Metal Ion Spin State—Lessons from Spin Crossover Complexes. *Crystals* **2016**, *6* (5), 58. https://doi.org/10.3390/cryst6050058.

(13) Rubensson, J.-E.; Hennies, F.; Pietzsch, A. High-Resolution Resonant Inelastic Soft X-Ray Scattering Applied to Liquids. *J. Electron Spectrosc. Relat. Phenom.* **2013**, *188*, 79–83. https://doi.org/10.1016/j.elspec.2013.01.012.

(14) Atak, K.; Golnak, R.; Xiao, J.; Pflüger, M.; Brandenburg, T.; Winter, B.; Aziz, E. F. Co(III) Protoporphyrin IX Chloride in Solution: Spin-State and Metal Coordination Revealed from Resonant Inelastic X-Ray Scattering and Electronic Structure Calculations. *Phys. Chem. Chem. Phys.* **2015**, *17* (5), 3409–3414. https://doi.org/10.1039/C4CP04703F.

(15) Atak, K.; Golnak, R.; Xiao, J.; Suljoti, E.; Pflüger, M.; Brandenburg, T.; Winter, B.; Aziz, E. F. Electronic Structure of Hemin in Solution Studied by Resonant X-Ray Emission Spectroscopy and Electronic Structure Calculations. *J. Phys. Chem. B* **2014**, *118* (33), 9938–9943. https://doi.org/10.1021/jp505129m.

(16) Neese, F. The ORCA Program System. *Wiley Interdiscip. Rev. Comput. Mol. Sci.* **2012**, *2* (1), 73–78. https://doi.org/10.1002/wcms.81.

(17) Masuda, Y.; Yamatera, H. Rotational Motions of the Tris(1,10-Phenanthroline) and Tris(2,2'-Bipyridine) Complexes of Ruthenium(II) and Cobalt(III) Ions in Solution. *J. Phys. Chem.* **1984**, *88* (16), 3425–3431. https://doi.org/10.1021/j150660a012.
(18) PURELAB® | ELGA LabWater http://www.elgalabwater.com/products/purelab (accessed Aug 30, 2017).
(19) Aziz, E. F.; Xiao, J.; Golnak, R.; Tesch, M. LiXEdrom: High Energy Resolution RIXS Station Dedicated to Liquid Investigation at BESSY II. *J. Large-Scale Res. Facil. JLSRF* **2016**, *2* (0), 80. https://doi.org/10.17815/jlsrf-2-85.
(20) Zhao, Y.; Truhlar, D. G. The M06 Suite of Density Functionals for Main Group Thermochemistry, Thermochemical Kinetics, Noncovalent Interactions, Excited States, and Transition Elements: Two New Functionals and Systematic Testing of Four M06-Class Functionals and 12 Other Functionals. *Theor. Chem. Acc.* **2007**, *120* (1–3), 215–241. https://doi.org/10.1007/s00214-007-0310-x.
(21) Weigend, F.; Ahlrichs, R. Balanced Basis Sets of Split Valence, Triple Zeta Valence and Quadruple Zeta Valence Quality for H to Rn: Design and Assessment of Accuracy. *Phys. Chem. Chem. Phys.* **2005**, *7* (18), 3297–3305. https://doi.org/10.1039/B508541A.
(22) Becke, A. D. Density-Functional Exchange-Energy Approximation with Correct Asymptotic Behavior. *Phys. Rev. A* **1988**, *38* (6), 3098–3100. https://doi.org/10.1103/PhysRevA.38.3098.
(23) Becke, A. D. Density-functional Thermochemistry. III. The Role of Exact Exchange. *J. Chem. Phys.* **1993**, *98* (7), 5648–5652. https://doi.org/doi:10.1063/1.464913.
(24) Roemelt, M.; Maganas, D.; DeBeer, S.; Neese, F. A Combined DFT and Restricted Open-Shell Configuration Interaction Method Including Spin-Orbit Coupling: Application to Transition Metal L-Edge X-Ray Absorption Spectroscopy. *J. Chem. Phys.* **2013**, *138* (20), 204101. https://doi.org/10.1063/1.4804607.
(25) Baerends, E. J.; Ellis, D. E.; Ros, P. Self-Consistent Molecular Hartree—Fock—Slater Calculations I. The Computational Procedure. *Chem. Phys.* **1973**, *2* (1), 41–51. https://doi.org/10.1016/0301-0104(73)80059-X.
(26) Dunlap, B. I.; Connolly, J. W. D.; Sabin, J. R. On Some Approximations in Applications of Xα Theory. *J. Chem. Phys.* **2008**, *71* (8), 3396–3402. https://doi.org/10.1063/1.438728.
(27) Vahtras, O.; Almlöf, J.; Feyereisen, M. W. Integral Approximations for LCAO-SCF Calculations. *Chem. Phys. Lett.* **1993**, *213* (5–6), 514–518. https://doi.org/10.1016/0009-2614(93)89151-7.
(28) Eichkorn, K.; Treutler, O.; Öhm, H.; Häser, M.; Ahlrichs, R. Auxiliary Basis Sets to Approximate Coulomb Potentials. *Chem. Phys. Lett.* **1995**, *240* (4), 283–290. https://doi.org/10.1016/0009-2614(95)00621-A.
(29) Eichkorn, K.; Weigend, F.; Treutler, O.; Ahlrichs, R. Auxiliary Basis Sets for Main Row Atoms and Transition Metals and Their Use to Approximate Coulomb Potentials. *Theor. Chem. Acc.* **1997**, *97* (1–4), 119–124. https://doi.org/10.1007/s002140050244.
(30) Weigend, F. Accurate Coulomb-Fitting Basis Sets for H to Rn. *Phys. Chem. Chem. Phys.* **2006**, *8* (9), 1057–1065. https://doi.org/10.1039/B515623H.
(31) Lenthe, E. van; Snijders, J. G.; Baerends, E. J. The Zero-order Regular Approximation for Relativistic Effects: The Effect of Spin–Orbit Coupling in Closed Shell Molecules. *J. Chem. Phys.* **1996**, *105* (15), 6505–6516. https://doi.org/10.1063/1.472460.
(32) Sinnecker, S.; Rajendran, A.; Klamt, A.; Diedenhofen, M.; Neese, F. Calculation of Solvent Shifts on Electronic G-Tensors with the Conductor-Like Screening Model (COSMO) and Its Self-Consistent Generalization to Real Solvents (Direct COSMO-RS). *J. Phys. Chem. A* **2006**, *110* (6), 2235–2245. https://doi.org/10.1021/jp056016z.

(33) Korotin, M. A.; Ezhov, S. Y.; Solovyev, I. V.; Anisimov, V. I.; Khomskii, D. I.; Sawatzky, G. A. Intermediate-Spin State and Properties of $LaCoO_3$. *Phys. Rev. B* **1996**, *54* (8), 5309–5316. https://doi.org/10.1103/PhysRevB.54.5309.

(34) Chen, J.-M.; Chin, Y.-Y.; Valldor, M.; Hu, Z.; Lee, J.-M.; Haw, S.-C.; Hiraoka, N.; Ishii, H.; Pao, C.-W.; Tsuei, K.-D.; et al. A Complete High-to-Low Spin State Transition of Trivalent Cobalt Ion in Octahedral Symmetry in $SrCo_{0.5}Ru_{0.5}O_{3-\delta}$. *J. Am. Chem. Soc.* **2014**, *136* (4), 1514–1519. https://doi.org/10.1021/ja4114006.

(35) Alvarez, S.; Cirera, J. How High the Spin? Allowed and Forbidden Spin States in Transition-Metal Chemistry. *Angew. Chem. Int. Ed.* **2006**, *45* (19), 3012–3020. https://doi.org/10.1002/anie.200503492.

(36) Potze, R. H.; Sawatzky, G. A.; Abbate, M. Possibility for an Intermediate-Spin Ground State in the Charge-Transfer Material $SrCoO_3$. *Phys. Rev. B* **1995**, *51* (17), 11501–11506. https://doi.org/10.1103/PhysRevB.51.11501.

(37) Stevens, J. S.; Newton, L. K.; Jaye, C.; Muryn, C. A.; Fischer, D. A.; Schroeder, S. L. M. Proton Transfer, Hydrogen Bonding, and Disorder: Nitrogen Near-Edge X-Ray Absorption Fine Structure and X-Ray Photoelectron Spectroscopy of Bipyridine–Acid Salts and Co-Crystals. *Cryst. Growth Des.* **2015**, *15* (4), 1776–1783. https://doi.org/10.1021/cg5018278.

(38) Stöhr, J. *NEXAFS Spectroscopy*; Springer Science & Business Media, 1992.

(39) Bedoya-Pinto, A.; Miralles, S. G.; Vélez, S.; Atxabal, A.; Gargiani, P.; Valvidares, M.; Casanova, F.; Coronado, E.; Hueso, L. E. Interface-Assisted Sign Inversion of Magnetoresistance in Spin Valves Based on Novel Lanthanide Quinoline Molecules. *Adv. Funct. Mater. 28* (16), 1702099. https://doi.org/10.1002/adfm.201702099.

(40) Magnuson, M.; Butorin, S. M.; Guo, J.-H.; Nordgren, J. Electronic Structure Investigation of CoO by Means of Soft X-Ray Scattering. *Phys. Rev. B* **2002**, *65* (20), 205106. https://doi.org/10.1103/PhysRevB.65.205106.

(41) Ament, L. J. P.; van Veenendaal, M.; Devereaux, T. P.; Hill, J. P.; van den Brink, J. Resonant Inelastic X-Ray Scattering Studies of Elementary Excitations. *Rev. Mod. Phys.* **2011**, *83* (2), 705–767. https://doi.org/10.1103/RevModPhys.83.705.

(42) Nia, N. Y.; Farahani, P.; Sabzyan, H.; Zendehdel, M.; Oftadeh, M. A Combined Computational and Experimental Study of the $[Co(Bpy)_3]^{2+/3+}$ Complexes as One-Electron Outer-Sphere Redox Couples in Dye-Sensitized Solar Cell Electrolyte Media. *Phys. Chem. Chem. Phys.* **2014**, *16* (23), 11481–11491. https://doi.org/10.1039/C3CP55034F.

(43) Weinhardt, L.; Weigand, M.; Fuchs, O.; Bär, M.; Blum, M.; Denlinger, J. D.; Yang, W.; Umbach, E.; Heske, C. Nuclear Dynamics in the Core-Excited State of Aqueous Ammonia Probed by Resonant Inelastic Soft x-Ray Scattering. *Phys. Rev. B* **2011**, *84* (10), 104202. https://doi.org/10.1103/PhysRevB.84.104202.

(44) Weinhardt, L.; Blum, M.; Fuchs, O.; Benkert, A.; Meyer, F.; Bär, M.; Denlinger, J. D.; Yang, W.; Reinert, F.; Heske, C. RIXS Investigations of Liquids, Solutions, and Liquid/Solid Interfaces. *J. Electron Spectrosc. Relat. Phenom.* **2013**, *188*, 111–120. https://doi.org/10.1016/j.elspec.2012.10.006.

(45) O'Shea, J. N.; Handrup, K.; Temperton, R. H.; Gibson, A. J.; Nicolaou, A.; Jaouen, N. Exploring Ultra-Fast Charge Transfer and Vibronic Coupling with N 1s RIXS Maps of an Aromatic Molecule Coupled to a Semiconductor. *J. Chem. Phys.* **2017**, *147* (13), 134705. https://doi.org/10.1063/1.4999135.

(46) Magnuson, M.; Yang, L.; Guo, J.-H.; Såthe, C.; Agui, A.; Nordgren, J.; Luo, Y.; Ågren, H.; Johansson, N.; Salaneck, W. R.; et al. Resonant Inelastic Soft X-Ray Scattering Spectra at the Nitrogen and

Carbon K-Edges of Poly(Pyridine-2,5-Diyl). *J. Electron Spectrosc. Relat. Phenom.* **1999**, *101–103*, 573–578. https://doi.org/10.1016/S0368-2048(98)00354-5.

(47) Löwdin, P.-O. On the Nonorthogonality Problem*. In *Advances in Quantum Chemistry*; Löwdin, P.-O., Ed.; Academic Press, 1970; Vol. 5, pp 185–199.

(48) Maganas, D.; DeBeer, S.; Neese, F. A Restricted Open Configuration Interaction with Singles Method To Calculate Valence-to-Core Resonant X-ray Emission Spectra: A Case Study https://pubs.acs.org/doi/full/10.1021/acs.inorgchem.7b01810 (accessed Oct 2, 2018). https://doi.org/10.1021/acs.inorgchem.7b01810.

(49) Maganas, D.; DeBeer, S.; Neese, F. Pair Natural Orbital Restricted Open-Shell Configuration Interaction (PNO-ROCIS) Approach for Calculating X-Ray Absorption Spectra of Large Chemical Systems. *J. Phys. Chem. A* **2018**, *122* (5), 1215–1227. https://doi.org/10.1021/acs.jpca.7b10880.

(50) Groot, F. de; Kotani, A. *Core Level Spectroscopy of Solids*; CRC Press, 2008.

(51) Maganas, D.; Roemelt, M.; Weyhermüller, T.; Blume, R.; Hävecker, M.; Knop-Gericke, A.; DeBeer, S.; Schlögl, R.; Neese, F. L-Edge X-Ray Absorption Study of Mononuclear Vanadium Complexes and Spectral Predictions Using a Restricted Open Shell Configuration Interaction Ansatz. *Phys. Chem. Chem. Phys.* **2013**, *16* (1), 264–276. https://doi.org/10.1039/C3CP52711E.

TOC

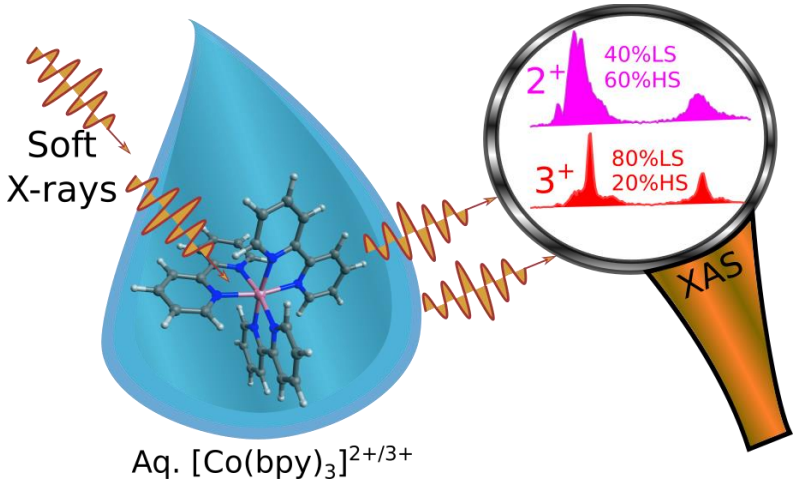

We report on the electronic structure of cobalt (II) tris-2,2'-bipyridine and cobalt (III) tris-2,2'-bipyridine in aqueous solution using resonant inelastic X-ray scattering (RIXS) spectroscopy at the Co L-edge and N K-edge resonances. For cobalt (II) tris-2,2'-bipyridine our combined experimental and computational study reveals ~40% low-spin and ~60% high-spin state components. Much stronger low-spin character is found for cobalt (III) tris-2,2'-bipyridine, ~80% low spin and ~20% high spin.